Measuring Local Atomic Structure Variations Through the Depth of Ultrathin (<20 nm) ALD Aluminum Oxide: Implications for Lithium-Ion Batteries

Nikhila C. Paranamana¹, Ryan Gettler², Henry Koenig¹, Stephen Montgomery-Smith³, Xiaoqing He^{4,5}, Matthias J. Young^{1,2,*}

Keywords: Atomic Layer Deposition, Pair Distribution Function, Molecular Structure, Electron Diffraction, Transmission Electron Microscopy

Abstract

Understanding the atomic structure of ultrathin (<20 nm) atomic layer deposition (ALD) coatings is critical to establish structure property relationships and accelerate the application of ALD films to stabilize battery interfaces. Previous studies have measured the atomic structure of nanoscale ALD films using cryogenic electron diffraction with a large (~200 nm) beam diameter. However, for ultrathin ALD coatings, these measurements provide only ensemble average structural information and cannot be used to directly measure differences in atomic structure through the depth of the ALD film. In this study, we localize the electron beam to a small (~ 5 nm) spot size using cryogenic scanning transmission electron microscope (STEM) and we collect electron diffraction data at multiple points along the depth of a 12 nm thick ALD AlO_x film deposited onto a CNT substrate without a contribution from the substrate. We couple these diffraction measurements with pair distribution function (PDF) analysis and iterative reverse Monte Carlomolecular statics (RMC-MS) modeling to compare atomic structure metrics at different positions in the film depth. We interpret the modeling results considering the 3D concentric cylindrical sample geometry of a CNT with uniform AlO_x coating. These measurements confirm a two-phase bulk/interface structural model proposed previously for ALD AlO_x and indicate that the interfacial layer at the CNT-AlO_x interface is 2.5 nm thick – five times larger than previously reported. This report demonstrates direct measurement of atomic structural variations across nanoscale material interfaces that is of broad interest for electrochemical applications and will help inform the use of ALD coatings to stabilize lithium-ion battery interfaces.

¹Department of Chemistry, University of Missouri, Columbia

²Chemical Engineering, University of Missouri, Columbia

³Department of Mathematics, University of Missouri, Columbia

⁴Electron Microscopy Core, University of Missouri, Columbia

⁵Mechanical and Aerospace Engineering, University of Missouri, Columbia

^{*}E-mail: matthias.young@missouri.edu

Introduction

Atomic layer deposition (ALD) is a gas phase vapor deposition technique which creates conformal nanoscale thin film coatings with atomic-scale control of film thickness using sequential surface reactions.^{1,2} ALD is a valuable technique for depositing ultra-thin (<20 nm) coating layers for a wide range of applications.^{3–7} Among these applications, ALD is of significant interest in energy storage devices, especially in lithium-ion and sodium-ion batteries. Recent studies have shown that ALD coatings enhance the shelf life, capacity, and energy density of these batteries. ALD is used to form nanoscale artificial solid electrolyte interfaces (SEI) at anode and to form protective thin film coatings on cathode electrode materials, to enhance cycling stability and to prevent degradation of the electrolyte and electrode material. 8-12 For example, ALD Al₂O₃ is a widely used as an artificial SEI material on hard carbon or graphitized anodes in sodium-ion and lithium-ion batteries. 13-18 However, the success of ALD aluminum oxide as a protective coating in battery applications is varied. In some instances, ALD aluminum oxide has been described to react with the electrolyte, generating phases with high Li-ion conductivity. 19,20 In other instances, thicker nanoscale films of ALD aluminum oxide have been found to exhibit low Li-ion conductivity and limit the charge rate of lithium-ion batteries. ²¹ ALD precursors have also been found to react with battery materials, yielding interphase layers that impact ion transport.^{22,23} Measuring the atomic structures of nanoscale ALD thin films is important to understand how ALD coatings react in battery environments and to control ALD film structures to rationally improve their performance in battery applications.

Commonly, characterization of ALD thin films has been performed by techniques such as X-ray photoelectron spectroscopy (XPS), Fourier transform infrared (FT-IR) spectroscopy, and electrochemical techniques, which give us only limited data to interpret the atomic structure. Recent work has employed more advanced characterization including solid-state nuclear-magnetic resonance (NMR),^{24–27} synchrotron techniques such as high-energy X-ray diffraction (HE-XRD),^{28–32}, X-ray absorption spectroscopy (XAS)^{33–35}, and ambient X-ray photoelectron spectroscopy,³⁶ and transmission electron microscopy (TEM).^{37,38} In a previous study, we examined the evolution of the atomic structure of amorphous ALD aluminum oxide (AlO_x) using *in situ* HE-XRD during ALD growth and established that ALD-AlO_x exhibits a two-phase structure, where the material close to substrate (substrate-AlO_x interface) and the material exposed to the atmosphere (surface) have a different atomic structure than the bulk material.³² Based on trends in the ensemble average structure as a function of thickness, these studies concluded that the surface and interfacial phases were on the order of 0.5 nm in thickness.

However, to date, no direct measurement of these interfacial phases has been performed to confirm that a different atomic structure exists at the interfaces relative to the bulk. Until recently, a more direct measurement of the local atomic structure of these films was not possible. Prior work has shown that by employing local electron diffraction within a TEM, the atomic structures of materials can be refined. However, TEM at ambient temperature can cause beam damage due to radiolytic decomposition and/or nano crystallite formation due to strong electron-material interactions. Recent work from our group demonstrated that inorganic metal oxides also undergo beam damage under ambient temperatures and that using cryogenic temperatures can

preserve the true atomic structure by limiting beam damage.³⁸ In this prior work, we examined the atomic structure of a ~10 nm thick ALD aluminum oxide layer on a multi-walled carbon nanotube (CNT) substrate using an electron diffraction spot size of ~200 nm. This large spot size encompassed a single ALD-coated CNT and did not allow for the direct measure of the spatial distribution of atomic structure through the depth the ALD film.³⁸

In the present study we employ cryogenic, local electron diffraction within a TEM to directly measure the atomic structure at the AlO_x surface and along the depth of an ALD AlO_x film to confirm previous results obtained from *in situ* synchrotron studies³² and wide-area electron diffraction TEM studies.³⁸ A CNT powder substrate is used in the present work for consistency with these prior studies. The hydroxyl-terminated CNTs employed here are a convenient low-Z substrate with a cylindrical sample geometry allowing us to localize the electron beam at various points along the cross-section of the ALD coating. Furthermore, understanding the local atomic structure of ALD aluminum oxide grown on sp² carbon substrates like CNTs is relevant to understand the behavior of ALD protective coatings on graphitic and carbon electrode materials in lithium-ion and sodium-ion batteries.^{13–18} Scanning transmission electron (STEM) microprobe mode was used to obtain a small (~5 nm) focused beam and allowed us to localize the beam on the AlO_x coating without contribution of the CNT substrate. Here we establish the atomic structure of ALD-AlO_x as a function of position through the depth of the ALD coating. This represents the highest spatial resolution diffraction measurement of the atomic structure of ALD AlO_x to date.

Results/Discussion

Figure 1(a) shows a colorized TEM image of ALD-AlO_x coated CNT. The AlO_x coating was deposited using 100 ALD cycles of trimethylaluminum and water at 177°C, yielding an alumina thickness of 12.46±0.19 nm in Figure 1a, consistent with an average growth rate of 1.2 Å/cycle at this deposition temperature.⁴⁵ We note that prior work observed a constant growth rate of ALD aluminum oxide from 1-100 ALD cycles on sp² carbon substrates under similar growth conditions. 46 To perform localized electron diffraction, we employed cryogenic scanning transmission electron microscopy (STEM) diffraction in microprobe mode using a Thermofisher TECNAI Twin F30 with a 0.1° convergence angle, producing a beam spot size of ~5 nm for the electron beam prior to diffraction.⁴⁷ For further measurement details, see the Materials and Methods section. For the data collected in Figure 1, the electron beam was first positioned on the outer surface of the AlO_x coating, and then repositioned to five additional spots moving inward toward the center of the CNT, as depicted with the red indicators in Figure 1a. The inset in Figure la shows a high angle annular dark field (HAADF) STEM image under the same imaging conditions as the STEM diffraction was performed. Local electron diffraction measurements were performed at each of the positions indicated in Figure 1a, corresponding to the raw diffraction data images in each panel of Figure 1b. The diffuse concentric rings observed in each panel of Figure 1b indicate that the AlO_x coating on the CNT is amorphous. In panels 5 and 6 of Figure 1b, we observe some diffraction spots which arise from the CNT, indicating texturing and crystalline ordering. Moving from the outer surface of the AlO_x (panel 1 of Figure 1b) through the AlO_x film toward the CNT/AlO_x interface (panel 5 of Figure 1b), we note visually discernable differences in the raw electron diffraction data due to the different structures of the AlO_x. The diffraction data in panel 1 (AlO_x surface) is grainy and shows some indications of asymmetry. The data becomes increasingly smooth and symmetric when considering panels 2, 3, and 4 in sequence.

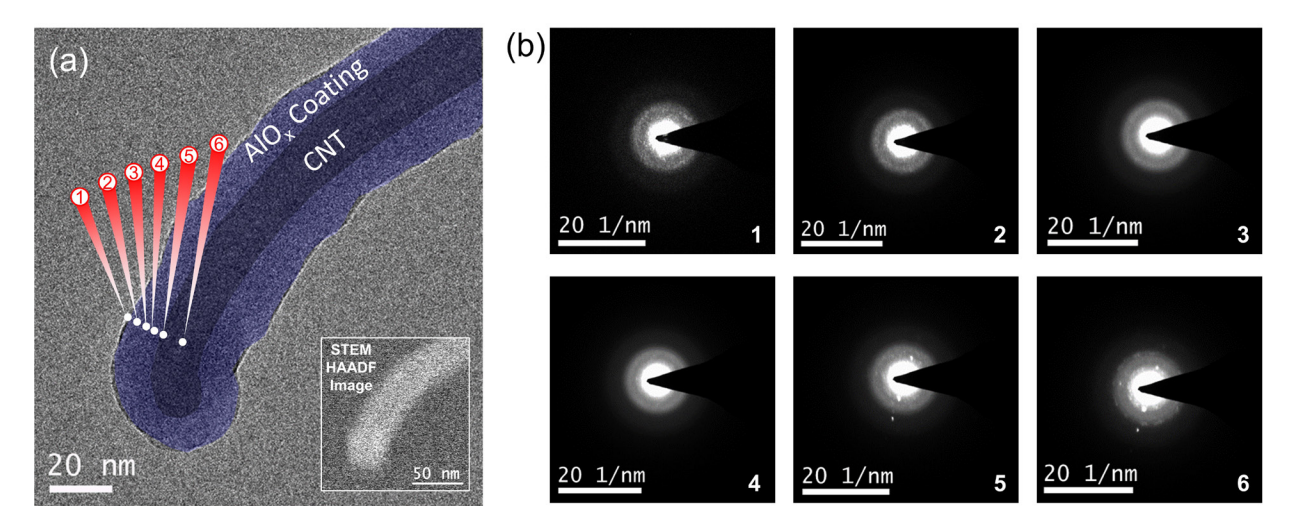


Figure 1. Cryogenic electron microscopy measurements including (a) colorized TEM bright field image of an AlO_x coated CNT showing the electron beam positioning to obtain diffraction patterns on different areas of the AlO_x. The STEM-HAADF image shows the focusing of the electron beam to obtain (b) raw diffraction images from the positions 1-6 along the AlO_x coated CNT indicated in panel (a).

In prior work, we demonstrated that cryogenic electron diffraction pair distribution function analysis (cryo-ePDF) could be used to measure the atomic structure of an AlOx coating formed on a CNT substrate using a large (~200 nm diameter) diffraction spot size and subtracting the contribution from the CNT substrate.³⁸ In Figure 2, we compare pair distribution functions (PDF or G(r)) obtained from large area diffraction (Figure 2a) and from local electron diffraction (Figure 2b) at multiple spots along the cross-section of the AlO_x film, both performed under cryogenic conditions. The large area PDF in Figure 2c was collected without using the STEM micro probe mode and the diffraction spot encompasses the AlO_x ALD coating and the CNT substrate as depicted in Figure 2a. The localized area PDF curve in Figure 2c was obtained by averaging three PDFs from different positions on the AlO_x coated CNT going through the surface to the bulk AlO_x. The corresponding error bars were calculated as the standard deviation of these PDFs. The large area G(r) agrees closely with the PDF calculated by averaging multiple localized diffraction measurements in Figure 2c, but does deviate beyond the standard deviation of the localized measurements in a few places, notably at pair distances of 1.36 Å, and at 2.45 Å. These pair distances correspond to the first and second C···C coordination shell, respectively, of the CNT substrate.⁴⁸ Although a background subtraction was performed to remove substrate contribution from the large area diffraction, residual evidence of these C···C features indicates that the CNT substrate subtraction procedure may not entirely remove C-C scattering.

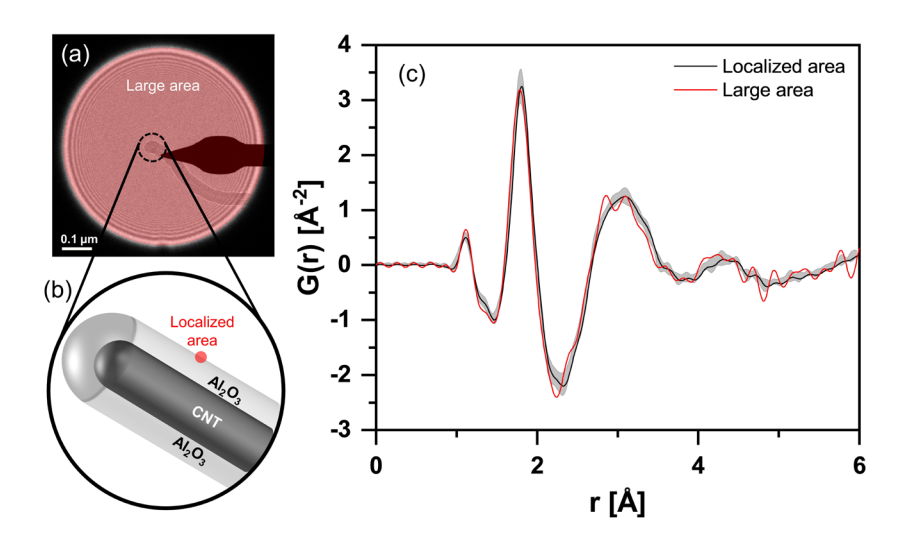


Figure 2. Comparison between (a) measurement of large area cryogenic electron diffraction²¹ relative to (b) localized area cryogenic electron diffraction employed in this work along with (c) comparison of G(r) curves obtained from the same AlO_x -coated CNT using these two diffraction modes. The localized area curve in (c) represents the average G(r) from diffraction measurements at three depths from the AlO_x surface and the shaded region around this average G(r) represents the standard deviation in the G(r) from these three measurement depths.

After establishing that the local electron diffraction agrees closely with large area electron diffraction under cryogenic temperatures, we wanted to confirm that cryogenic temperatures are needed to preserve the material structure during electron beam exposure, as identified using large area diffraction in prior work.²¹ In this prior work, we observed significant beam damage at ambient temperature using an electron beam exposure time of 10 s at an electron flux of 7.28 e-/Å²/s, corresponding to a total dose of 72.8 e-/Å². ²¹ Here, we employ a similar beam current, but localize the beam to an area ~1600 times smaller and use a 2 s exposure rather than a 10 s exposure. From this, we estimate that the electron fluence is approximately two orders of magnitude larger here. We therefore expect that electron beam damage would be more significant than when using large area diffraction, as confirmed from the data in Figure 3. Figure 3 shows a comparison of PDFs generated from local electron diffraction at the outer AlO_x surface under ambient and cryogenic temperatures. The cryogenic temperature PDF in Figure 3 represents the average of PDFs from three electron diffraction measurements at the outer surface of the AlO_x and the grey area corresponds to the standard deviation from these triplicate measurements. Here, we compare the surface measurements under cryogenic and ambient temperature conditions because the surface is expected to reconfigure most readily under electron beam exposure. We note in Figure 3 that the PDF measured under ambient temperature conditions is significantly different from the PDF data under cryogenic temperature conditions. We observe a clear deviation of the peaks at ~1.4 Å, 1.8 Å, 2.2 Å and 2.9 Å. We calculate a mean percent error value for |G(r)| > 0.2 of 23 % for the ambient data relative to the cryogenic data. Here, the convergence angle, electron beam exposure, and beam localization are all equivalent between the ambient and cryogenic measurement conditions. The differences between the PDFs obtained under ambient and cryogenic conditions indicate changes in the atomic structure present on the surface under ambient measurement

conditions. These atomic structure differences may arise from either beam damage or environmental effects. As reported in prior work, the electron beam exposure introduces charged defects in AlO_x, causing amorphization under low electron doses, and crystallization under higher electron doses. ^{38,41,42} In addition to this beam damage effect, the use of ambient temperature conditions during ePDF measurements under vacuum is expected to allow for recombination of surface R-OH groups to form gaseous H₂O and R-O-R surface groups. ^{45,49–54} We expect that both of these effects play a role in the differences between PDFs obtained under cryogenic and ambient conditions in Figure 3. Overall, the data in Figure 3 indicate that the use of cryogenic conditions is necessary to preserve and measure the true material structure present on the surface of AlO_x.

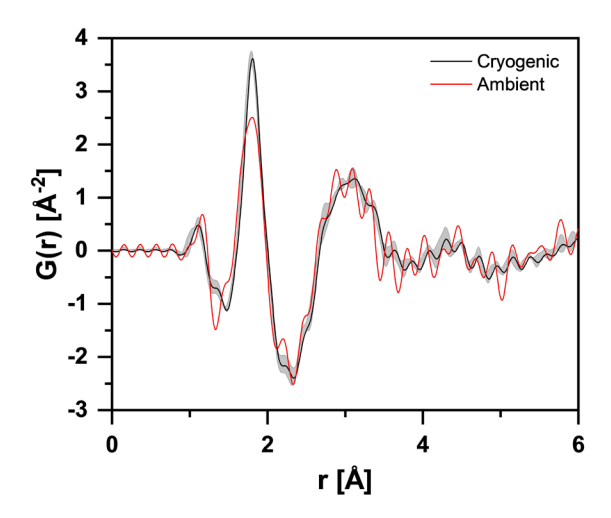


Figure 3. Comparison of the G(r) curves obtained from localized electron diffraction at the surface of the AlO_x coating under cryogenic liquid nitrogen temperatures (black) and ambient temperatures (red). The G(r) curve for cryogenic temperatures is the average from three diffraction measurements and the shaded area around the cryogenic G(r) curve represents the standard deviation from these triplicate measurements.

After demonstrating the ability to localize the electron beam and confirming the need to employ cryogenic conditions to mitigate beam damage, we employ this local electron diffraction to measure the atomic composition as a function of position along the cross-section of the ALD aluminum oxide coating under cryogenic conditions. In Figure 4a we present a schematic of the process of localized electron diffraction performed on ALD-AlO_x coated CNT for subsequent analysis. Four main regions were analyzed: (1) the outer surface of the AlO_x (electron beam centered on AlO_x surface), (2) bulk AlO_x (electron beam centered on the midplane of the AlO_x film, (3) the inner surface of the AlO_x near the CNT interface (electron beam centered as close as possible to the CNT without observing CNT diffraction signal) and (4) the bulk CNT with AlO_x coating (electron beam centered on the center axis of the CNT substrate). Figure 4b shows the pair distribution functions obtained at these four different depths. Each G(r) curve in Figure 4 is the average of three PDF measured at the same depth, but at varying positions along the perimeter of the AlO_x coating on an individual CNT, and these average PDFs are used for further analysis below. The dominant peak at a pair distance of ~1.8 Å for positions 1-3 corresponds to Al-O pairs. In Figure 4b, we observe a qualitatively different PDF with more numerous and well-defined peaks

at the outer AlO_x surface (position 1) as compared with deeper within the bulk AlO_x (positions 2 and 3). This suggests that the AlO_x material at the outer surface of the AlO_x layer contains more structural ordering than the bulk AlO_x layer. Although position 1 exhibits more structural order than positions 2 and 3, all three measurements on the AlO_x layer (1-3) lack long range order for pair distances > 5 Å. This further validates previous indications that ALD AlO_x is amorphous, ^{32,38,45,52,55,56} even over short-range (5 nm diameter spot size) regions. We note that at position 4, the electron beam is passing through both the CNT and the Al₂O₃ coating, leading to peaks from both the CNT and AlO_x coating in Figure 4b. The peak at a pair distance of 1.4 Å at position 4 is consistent with C-C bonds within the CNT substrate, and the peak at a pair distance at 2.4 Å at position 4 is consistent with the second-coordination sphere of C···C pairs within CNTs. 48,57 Because of the contribution of the CNT, PDF data collected at position 4 was not analyzed further. The CNT peaks at 1.4 Å and 2.4 Å are not observed in the PDF data from the other positions (1-3) because the electron beam is focused locally onto the AlO_x layer. This allows us to analyze the atomic structure of the aluminum oxide coating layer without needing to subtract the contribution from the substrate, as is necessary using large area electron diffraction reported in previous work.³⁸

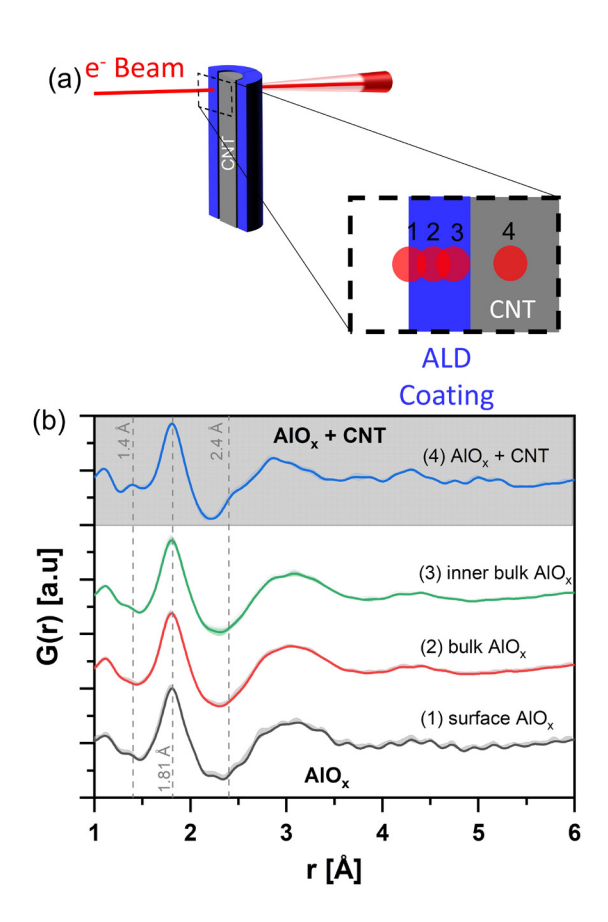


Figure 4. (a) A schematic depiction of electron beam diffraction performed at four depths into the AlO_x coated CNT, as well as (b) corresponding G(r) curves, each representing the average of three diffraction measurements at each of four depths: (1) the surface AlO_x , (2) bulk AlO_x , (3) AlO_x near

the interface of CNT, and (4) center of the CNT with the AlO_x coating to identify structural differences of AlO_x at different positions. The shaded regions around each G(r) curve in (b) represent the standard deviation in the G(r) from the triplicate diffraction measurements.

In addition to the qualitative analysis of how atomic structure changes as a function of position along the AlO_x layer discussed surrounding Figure 4, we also performed RMC modeling to derive atomistic structural models from the experimental PDF data. For this analysis we employed the recursive RMC-MS modeling approach reported recently³¹ and employed the aluminum oxide ReaxFF pair potential developed by Hong et. al.⁵⁸ An example PDF from RMC-MS modeling with the corresponding experimental PDF data is depicted in Figure 5a for the surface AlO_x (position 1). We find that the RMC-MS model reduces χ^2 error and reduces the cohesive energy relative to RMC-only modeling for all modeling conditions. For the example data for position 1 depicted in Figure 5a, the χ^2 for the RMC-MS model fit was 91.64. This value was 108.91 for RMC-only modeling. Likewise, the cohesive energy for position 1 depicted in Figure 5a, was -121.85 kcal/mol for the RMC-MS model fit and was -115.75 kcal/mol for the RMC-only fit. This highlights that the RMC-MS approach provides more physically realistic atomic structure models with equivalent fit to experimental data, as reported previously.³¹ Figure 5b shows the resulting RMC-MS atomistic structural model for ALD-AlO_x for the bulk (position 2). The *.xyz files for the RMC-MS model structures of AlO_x at positions 1, 2, and 3 are all included in the Supporting Information (SI) Section A.

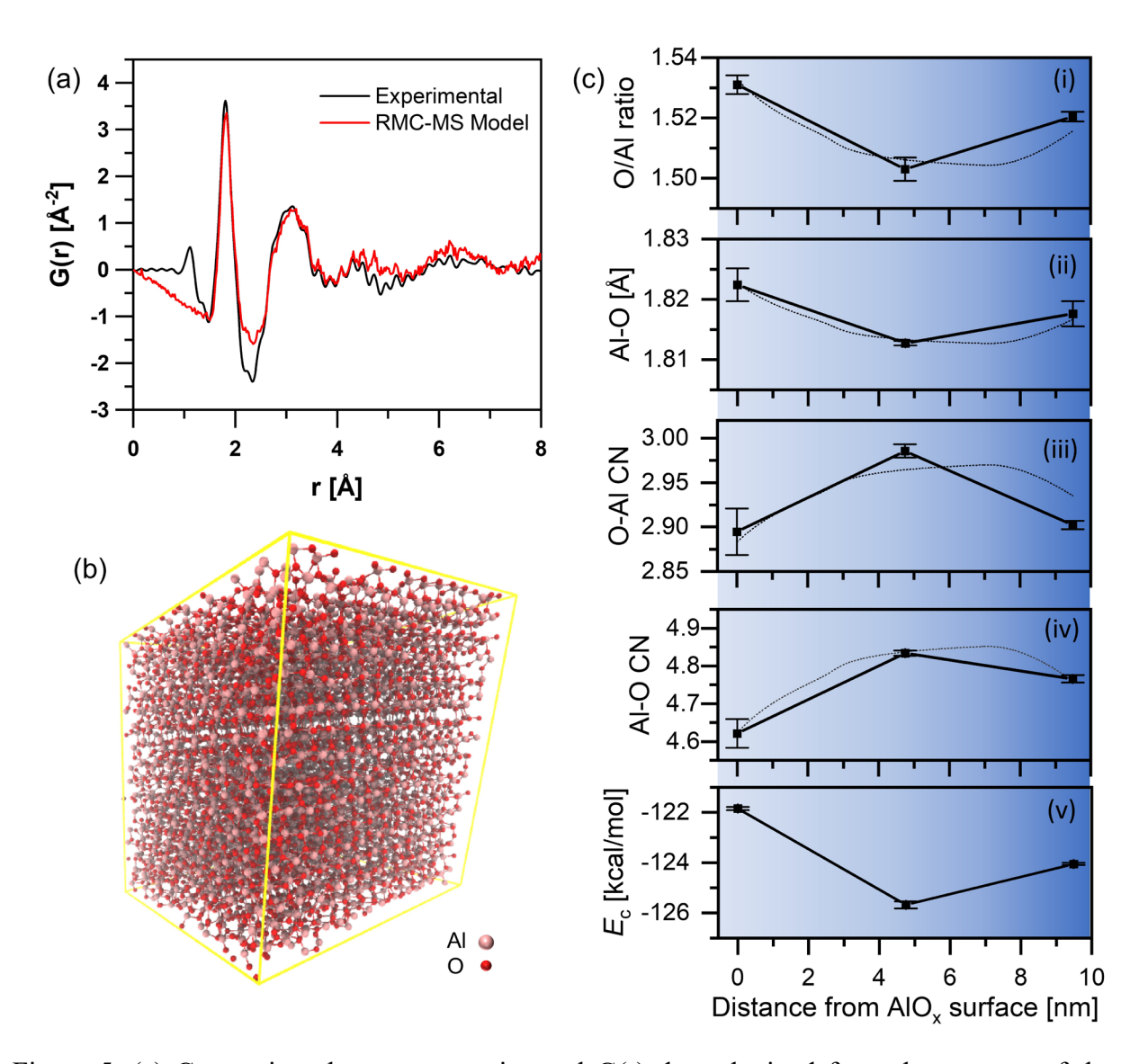


Figure 5. (a) Comparison between experimental G(r) data obtained from the average of three diffraction measurements at the surface of AlO_x and G(r) from the RMC-MS model fit. RMC-MS modeling yielding (b) atomistic structural model for AlO_x within the bulk AlO_x (position 2). In (c), for three different depths into the coated CNT (distances from AlO_x surface), we report structural metrics including (i) O/Al ratio, (ii) Al-O bond length, (iii) O-Al CN, (iv) Al-O CN and (v) cohesive energies of AlO_x, all derived from RMC-MS model structures fitted to average PDFs at each depth. The expected trends in these metrics for a two-phase material structure are indicated by the dashed lines in each panel. The error bars in (c) represent the standard deviation from three RMC-MS model fits for the average PDF obtained at each depth.

We then analyzed the atomic structures derived from RMC-MS modeling at positions 1, 2, and 3 to understand how local atomic structure features change as a function of position along the cross-section of the AlO_x coating. Figure 5c depicts trends in structural metrics for positions 1-3 derived from RMC-MS model structures, including (i) O/Al ratio, (ii) average Al-O bond length, (iii) Al-O coordination number (CN), (iv) O-Al CN, and (v) cohesive energy. The dashed lines in each

panel correspond to a two-phase model fit as discussed in more detail below. The average Al-O bond length was modeled to be 1.822Å for surface AlO_x (position 1). The bulk AlO_x (position 2) shows a smaller bond length of 1.813 Å. This value increases when moving towards the AlO_x near the CNT (position 3). This indicates that the Al-O bond length is longer when near the CNT surface. In Figure 5c.iv, the average Al-O CN measured at the surface of the AlO_x coating (position 1) is 4.621 and is 4.765 near the CNT interface (position 3). The bulk AlO_x (position 2) shows a higher coordination number of 4.833. The bulk AlO_x coordination number is consistent with a blend of tetrahedral and octahedral aluminum centers, as expected for the θ -Al₂O₃ crystal structure. The lower coordination numbers at the interfaces suggest that Al atoms at the CNT and vacuum interfaces are undercoordinated, e.g., with three oxygen atoms as suggested by the Orich surface model proposed previously. The lower coordinated is a suggested by the Orich surface model proposed previously.

Terminal oxygen atoms present at interfaces are also expected to drive the O-Al CN at the surface of the AlO_x lower vs. the bulk due to -(OH)₂ and -OH groups present at the surface. Indeed, we find that the O-Al CNs (Figure 5c.iii) measured at the outer surface of AlO_x coating (position 1) and at the CNT interface (position 3) are lower (2.894 and 2.092, respectively) than the O-Al CN measured at the bulk position (2.985 O-Al CN at position 2). At the outer surface of the AlO_x coating the surface is expected to be rich in oxygen due to terminal –(OH)₂ and -OH groups. Likewise, the CNT-AlO_x interface is expected to be rich in oxygen due to R-C-OH nucleation sites. Indeed, Figure 5c.i shows a higher O:Al stoichiometry at the surface of the AlO_x coating and at the CNT-AlO_x interface. In Figure 5c.v, we report the cohesive energy following RMC-MS modeling for each model structure. We find that the bulk structure is more thermodynamically favorable than the structure present at the surface of the AlO_x. The surfaces and interfaces contain high-energy dangling bonds and undercoordinated atoms, which we expect are the origin of higher energy structures at the interfaces vs. the bulk.

We note that although we focused the electron beam down to a \sim 5 nm spot size for the measurements reported in this work, this beam diameter is still \sim 10× larger than the expected thickness of \sim 0.5 nm for the O-rich interface layer present on the surface of the AlO_x . Additionally, when the electron beam is localized at any position along the AlO_x coating, the electron beam intersects with a volume of the AlO_x from the surface, as well as the bulk structure, as depicted in Figure 6a. To capture this physical picture and more quantitatively interpret the trends in atomic structure metrics in Figure 5, we constructed a 3D model of the electron beam interacting with a two-phase AlO_x -ALD coating layer consistent with Figure 6a and calculated the fraction of volume of the electron beam interacting with each of three phases (surface, bulk, and AlO_x -CNT interface). A python script to calculate the volume fraction of surface vs. bulk layers sampled as function of position of the electron beam is provided in the supplemental information along with a mathematical derivation of the equations used in this model. We used this python script to calculate weighted averages of the expected contribution from bulk and boundary layers using the values outlined below.

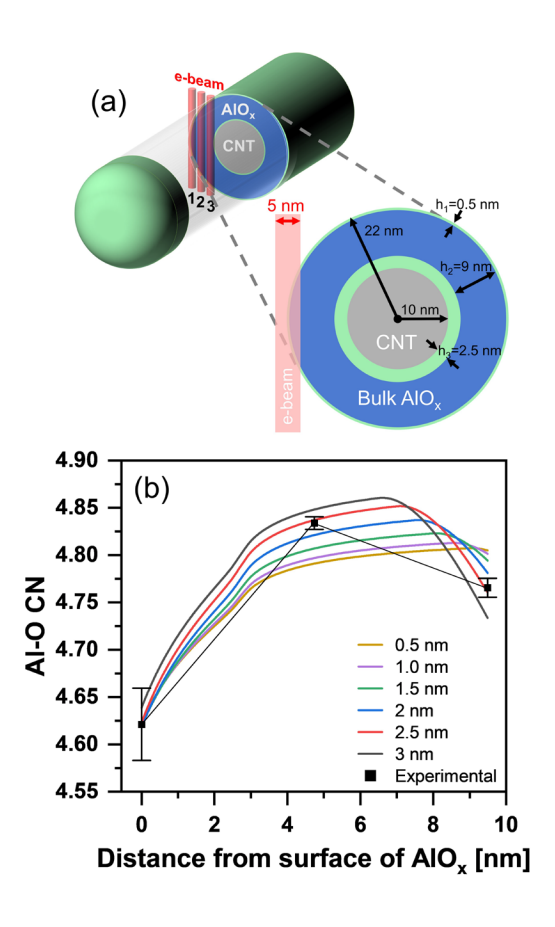


Figure 6: (a) A schematic depiction of the electron beam passing through the coated CNT during diffraction, along with (b) a comparison of the Al-O bond coordination numbers obtained by RMC-MS with different model traces for the expected Al-O CN for varying thicknesses of the interface region at the CNT surface (h₃).

The specifics of this model are depicted in Figure 6a, where the CNT is taken to be a cylinder of 20 nm diameter and the AlO_x layer is taken to be 12 nm in total thickness, in line with TEM measurements reported above in Figure 1. This AlO_x layer is assumed to be comprised of three distinct layers: (1) an interfacial phase at outer surface of the AlO_x , (2) a bulk phase, and (3) an interfacial phase at the inner surface of the AlO_x film adjacent to the CNT surface. Here, we assume the interfacial phase at the outer surface of the AlO_x is $h_1 = 0.5$ nm thick based on HE-XRD measurements, 32 and we allow the thickness of the interfacial phase at the inner surface of the AlO_x adjacent to the CNT, h_3 , to vary. The thickness of the bulk phase, h_2 , is adjusted such that the total AlO_x film thickness remains constant at $h_T = h_1 + h_2 + h_3 = 12$ nm. We take the diameter of the electron beam to be 5 nm and assume that the electron beam axis is positioned perpendicularly to the axis of the CNT beam at a distance, c, offset from the CNT center axis. We then calculate the volume fraction of the interfacial phases (corresponding to h_1 and h_3) that is sampled as a function of beam position, c. See SI Section B for more detail.

Using the resulting volume fractions, and assuming the atomic structure within h_1 is equivalent to the atomic structure within h_3 , we calculate the contribution from each of the two interfacial layers to predict the metrics reported in Figure 5 as a function of beam position, as indicated on each

panel from Figure 5c.i-iv using dashed lines. The dashed lines reported in Figure 5 are the result of recursive fitting to yield h_3 =2.5 nm and values of structural metrics (O:Al, Al-O bond length, Al-O CN, and O-Al CN) for each layer. This recursive fitting yields an interfacial boundary layer thickness of h_3 = 2.5 nm with structural metrics of O:Al = 1.594, Al-O bond length = 1.844 Å, Al-O CN = 4.122, and O-Al CN = 2.692 for both regions of h_1 and h_3 . Correspondingly, this fitting yielded h_2 = 9.0 nm for the bulk AlO_x layer with O:Al = 1.500, Al-O bond length = 1.811 Å, Al-O CN = 4.884 and O-Al CN = 2.982. These values for bulk structure metrics agree closely with previous results of Al-O CN=4.71, O-Al CN=2.97 from synchrotron HE-XRD measurements.³²

The calculated traces obtained for the Al-O CN upon varying the h₃ thickness and each of the structural metrics are shown in Figure 6b. As mentioned above, the best fit curve for RMC-MS data is obtained when the CNT-AlO_x interface is taken to be 2.5 nm in thickness. Here, we note that values of $h_3=3.0$ nm or $h_3=2.0$ nm yield a 31% and 73% increase in fitting error, respectively, across all structural metrics. In the analysis of previous ex situ HE-XRD measurements, it was assumed that h₁=h₃ in the absence of data to the contrary.³² However, here, using more precise measurements at different depths along the AlO_x surface, the thickness of the interfacial layer near the surface of the CNT (h₃) was found to be 2.5 nm, five times thicker at than h₁ of 0.5 nm. We expect that this difference in height between h₁ and h₃ arises from nucleation delay occurred on the CNT substrate which contains sparsely functionalized hydroxyl groups, such that a thickness of more than >2 nm is required to establish a bulk layer. This interpretation is supported by a higher O:Al, lower Al-O CN and lower O-Al CN for the interfacial layers compared to the bulk. Using the fractions of volume sampled as a function of position and total energies from the final molecular statics (MS) modeling step, we calculate a cohesive energy for the surface layer of -112.95 kcal/mol (-24.48 eV), and a bulk cohesive energy of -126.41 kcal/mol (-27.40 eV). These values generally agree with values calculated from density functional theory of -29.85 eV for a 2D monolayer of Al₂O₃ and -32.8 eV for bulk α-Al₂O₃, indicating a ~10% less negative cohesive energy for the surface of AlO_x. 60,61

Conclusions

This report demonstrates the direct measurement of the atomic structure along the depth of a 12 nm thick ALD AlO_x film with ~5 nm spatial resolution. We identify a bulk amorphous AlO_x structure consistent with a blend of tetrahedral and octahedral AlO_x as described previously. Our results also confirm the presence of a 0.5 nm-thick undercoordinated structure on the outer surface of the AlO_x, as suggested in prior work. However, we identify that the CNT substrate alters the AlO_x structure nearest the CNT substrate to a distance of ~2.5 nm into the AlO_x, five times thicker than indicated by bulk ensemble-average measurements. The structural metrics in this interfacial region near the CNT are consistent with a lower-density and undercoordinated AlO_x material. We attribute this to sparse nucleation on hydroxylated CNTs, $^{46,62-65}$ giving rise to a lower-density layer in this region. The distribution of atomic structures within a 12 nm thick alumina layer we report here is expected to inform conceptual models to explain how nanoscale ALD aluminum oxide of different thicknesses performs in lithium-ion battery environments. For example, the specific atomic structural models we provide will allow for follow-on theoretical studies to predict how nanoscale ALD aluminum oxide reacts with lithium-ion battery electrolytes under applied anodic

and cathodic voltages. Furthermore, the lower density interfacial layer we measure at the CNT interface is expected to impact the thermal, electrical, and mechanical properties of this ALD-substrate interface, e.g., reducing the dielectric constant and thermal conductivity. These materials properties are critical to semiconductor device manufacturing and are expected to inform the use of ALD in, for example, graphene-based nanoelectronics. Similarly, understanding the interfacial structure of ALD aluminum oxide is relevant for improving the electronic properties of advanced semiconductor gate stacks. Pulliding on the approaches and analysis established in this study, future work will examine how different substrates and surface hydroxyl densities influence the atomic structure of ALD films near the substrate surface.

Previous reports have identified that the substrate material drives the bulk atomic structure of ALD coatings, for example manganese oxide ALD leaches sodium from soda lime glass substrates and aluminum oxide ALD induces redox in ruthenium substrates. This substrate reactivity is especially prominent when applying ALD coatings to reactive battery materials. Using the methods outlined in this report, we expect to be able to quantitatively measure how and to what depth the substrate (e.g. battery material powders) influences the atomic structure of the ALD film at the substrate/coating interface. We emphasize that the electron diffraction PDF measurements we employ here are ideal for disordered, nanocrystalline and amorphous materials, where direct STEM imaging of atom positions is not possible. The methods and analysis demonstrated in this work are also relevant outside the ALD community and can be used to measure atomic structure across many material interfaces in semiconductors, batteries, catalysts, and solar cells. Furthermore, next-generation TEM instrumentation including direct electron detectors, and 4D-STEM-PDF will allow for rapid measurement of atomic structure across material interfaces with higher spatial resolution and minimal beam damage.

Materials and Methods

Preparation of TEM samples

Hydroxyl-terminated multiwalled carbon nano tubes (CNTs) with a nominal diameter of 20 nm were used as the substrate to deposit AlO_x. A small amount of CNTs were loaded onto a TEM lacey carbon copper grid (200 mesh) using a custom TEM grid holder described previously.³⁸ This holder containing the TEM grid loaded with CNTs was placed directly in the ALD reactor to form ALD films on the CNT substrate for characterization.

Atomic layer deposition

A custom hot walled viscous-flow reactor was used to deposit AlO_x by thermal ALD. Ultra-high purity argon (Ar, 99.999%, Airgas) was used as the carrier gas at a flow rate of 200 sccm. AlO_x depositions were carried out at a substrate temperature of 177°C. Trimethylaluminum (TMA, 98%, Strem) was used as the aluminum precursor source and de-ionized water (H₂O) as the oxidant. All the precursors used were held at ambient temperature and dosed using a virtual valve configuration. Sequential timed dosing of TMA and H₂O followed by Ar purge after every dose was programmed using LabVIEW, with 1 s dose and 10 s purge for both precursors. This sequential dosing and purge of TMA and H₂O were continued for 100 cycles to obtain a final AlO_x thickness of 12 nm.

Electron Diffraction under STEM microprobe mode

The TEM grid was loaded into the Gatan side entry cryo TEM holder 626 at the ambient temperature and liquid nitrogen was gently poured into the reservoir in the loading station to cool down the grid. A steady reading of -194 C on the holder temperature controller was reached before inserting the TEM holder into the TEM. The cryo holder was loaded at least 2 hours prior to data collection to minimize the effect of the sample drift. A Thermofisher Tecnai G2 F30 TEM was used for both TEM imaging and STEM diffraction measurements at 200 kV. A spot size 10 and C2 condenser lens aperture of 50 µm was used for STEM image and diffraction measurement operated in the microprobe mode where the beam convergent semi angle is measured to be around 1.82 mrad (0.103 degree) based on the electron diffraction pattern collected along [110] Si under the same imaging settings used in this study. The nominal camera length for electron diffraction measurements was 100 mm, which was calibrated using the Si standard for data processing as described below. Between diffraction measurements, a STEM-HAADF image was acquired prior to the next data point collection to ensure the beam had not drifted.

Integration of 2D electron diffraction data to obtain PDFs

The GSASII software package 82 was used to process 2D electron diffraction images to obtain the powder diffraction patterns. A calibrated camera length of 186.3 mm was found using the diffraction pattern of a Si standard considering the wavelength of an electron as 0.02508 Å (including relativistic effects) at the accelerating voltage of 200 kV used in this study. The diffraction images were integrated using a Q range of $Q_{min}=1.5$ and $Q_{max}=35$. The PDFgetX3 software package 83 was used to obtain the fourier transform of the powder diffraction patterns to obtain the pair distribution function.

RMC-MS Computational Modeling

Structural and thermodynamic properties of ALD-grown alumina were modeled using a previously developed hybrid RMC-MS technique.³¹ Briefly, two million RMC translations were used to fit an input structure (HM space group *C2/m*12, edge length 40 Å) to the experimental PDF, followed immediately by an energy minimization using MS. This cycle was repeated five times, i.e., five RMC steps of two million translations each separated by four MS relaxations. RMC calculations were performed using the fullRMC⁸⁴ package, with CN values for Al-O pairs constrained to a value from 4-7 within a distance of 1.5-2.3 Å. Additional constraints are given in Table 1. MS calculations were implemented in LAMMPS⁸⁵ using a ReaxFF pair potential developed by Hong et. al.⁵⁸ Structural metrics were derived from the final RMC-MS structures using the ISAACS software package.⁸⁶

Table 1: Minimum pair distance constraints

1 tible 1	· minimum pan	i distanc	distance constraints	
Pair	Al-Al	0-0	Al-O	
r (Å)	2.1	1.2	1.5	

Acknowledgements

NCP and MJY thank the Electron Microscopy Core (EMC) and the Office of Research at the University of Missouri for financial support through the Excellence in Electron Microscopy award. MJY acknowledges support from faculty start-up funds from the University of Missouri, and partial support from the National Science Foundation Division of Chemical, Bioengineering, Environmental and Transport Systems (CBET) through award number 2219060.

References

- (1) Johnson, R. W.; Hultqvist, A.; Bent, S. F. A Brief Review of Atomic Layer Deposition: From Fundamentals to Applications. *Materials Today* **2014**, *17* (5), 236–246. https://doi.org/10.1016/j.mattod.2014.04.026.
- (2) George, S. M. Atomic Layer Deposition: An Overview. *Chemical Reviews* **2010**, *110* (1), 111–131. https://doi.org/10.1021/cr900056b.
- (3) Sheng, J.; Lee, J.-H.; Choi, W.-H.; Hong, T.; Kim, M.; Park, J.-S. Review Article: Atomic Layer Deposition for Oxide Semiconductor Thin Film Transistors: Advances in Research and Development. *Journal of Vacuum Science & Technology A* **2018**, *36* (6), 060801. https://doi.org/10.1116/1.5047237.
- (4) Zhao, Z.; Kong, Y.; Zhang, Z.; Huang, G.; Mei, Y. Atomic Layer–Deposited Nanostructures and Their Applications in Energy Storage and Sensing. *Journal of Materials Research* **2020**, *35* (7), 701–719. https://doi.org/10.1557/jmr.2019.329.
- (5) O'Neill, B. J.; Jackson, D. H. K.; Lee, J.; Canlas, C.; Stair, P. C.; Marshall, C. L.; Elam, J. W.; Kuech, T. F.; Dumesic, J. A.; Huber, G. W. Catalyst Design with Atomic Layer Deposition. *ACS Catalysis* **2015**, *5* (3), 1804–1825. https://doi.org/10.1021/cs501862h.
- (6) Lin, H.-C.; Chang, Y.-L.; Han, Y.-Y.; Yang, K.-C.; Chen, M.-C. Atomic Layer Deposited Al2O3 Films on NiTi Shape Memory Alloys for Biomedical Applications. *Procedia Manufacturing* **2019**, *37*, 431–437. https://doi.org/10.1016/j.promfg.2019.12.070.
- (7) Paranamana, N. C.; He, X.; Young, M. J. Atomic Layer Deposition of Thin-Film Sodium Manganese Oxide Cathode Materials for Sodium Ion Batteries. *Dalton Transactions* **2021**, 50 (48), 18128–18142. https://doi.org/10.1039/d1dt03479k.
- (8) Su, Y.; Cui, S.; Zhuo, Z.; Yang, W.; Wang, X.; Pan, F. Enhancing the High-Voltage Cycling Performance of LiNi 0.5 Mn 0.3 Co 0.2 O 2 by Retarding Its Interfacial Reaction with an Electrolyte by Atomic-Layer-Deposited Al 2 O 3. *ACS Applied Materials & Interfaces* **2015**, 7 (45), 25105–25112. https://doi.org/10.1021/acsami.5b05500.
- (9) Lin, C.-F.; Kozen, A. C.; Noked, M.; Liu, C.; Rubloff, G. W. ALD Protection of Li-Metal Anode Surfaces Quantifying and Preventing Chemical and Electrochemical Corrosion in Organic Solvent. *Advanced Materials Interfaces* **2016**, *3* (21), 1600426. https://doi.org/10.1002/admi.201600426.
- (10) Alvarado, J.; Ma, C.; Wang, S.; Nguyen, K.; Kodur, M.; Meng, Y. S. Improvement of the Cathode Electrolyte Interphase on P2-Na 2/3 Ni 1/3 Mn 2/3 O 2 by Atomic Layer

- Deposition. *ACS Applied Materials & Interfaces* **2017**, *9* (31), 26518–26530. https://doi.org/10.1021/acsami.7b05326.
- (11) Woo, J. H.; Trevey, J. E.; Cavanagh, A. S.; Choi, Y. S.; Kim, S. C.; George, S. M.; Oh, K. H.; Lee, S.-H. Nanoscale Interface Modification of LiCoO 2 by Al 2 O 3 Atomic Layer Deposition for Solid-State Li Batteries. *Journal of The Electrochemical Society* 2012, *159* (7), Al120–Al124. https://doi.org/10.1149/2.085207jes.
- (12) Kazyak, E.; Wood, K. N.; Dasgupta, N. P. Improved Cycle Life and Stability of Lithium Metal Anodes through Ultrathin Atomic Layer Deposition Surface Treatments. *Chemistry of Materials* **2015**, *27* (18), 6457–6462. https://doi.org/10.1021/acs.chemmater.5b02789.
- (13) Zhu, S.; Liu, J.; Sun, J. Precise Growth of Al2O3/SnO2/CNTs Composites by a Two-Step Atomic Layer Deposition and Their Application as an Improved Anode for Lithium Ion Batteries. *Electrochimica Acta* **2019**, *319*, 490–498. https://doi.org/10.1016/j.electacta.2019.07.027.
- (14) Yu, C.; Li, Y.; Ren, H.; Qian, J.; Wang, S.; Feng, X.; Liu, M.; Bai, Y.; Wu, C. Engineering Homotype Heterojunctions in Hard Carbon to Induce Stable Solid Electrolyte Interfaces for Sodium-ion Batteries. *Carbon Energy* **2022**, No. February, 1–13. https://doi.org/10.1002/cey2.220.
- (15) Wang, C.-C.; Su, W.-L. Ultrathin Artificial Solid Electrolyte Interface Layer-Coated Biomass-Derived Hard Carbon as an Anode for Sodium-Ion Batteries. *ACS Applied Energy Materials* **2022**, *5* (1), 1052–1064. https://doi.org/10.1021/acsaem.1c03425.
- (16) Lu, H.; Chen, X.; Jia, Y.; Chen, H.; Wang, Y.; Ai, X.; Yang, H.; Cao, Y. Engineering Al2O3 Atomic Layer Deposition: Enhanced Hard Carbon-Electrolyte Interface towards Practical Sodium Ion Batteries. *Nano Energy* **2019**, *64* (July), 103903. https://doi.org/10.1016/j.nanoen.2019.103903.
- (17) Jung, Y. S.; Lu, P.; Cavanagh, A. S.; Ban, C.; Kim, G. H.; Lee, S. H.; George, S. M.; Harris, S. J.; Dillon, A. C. Unexpected Improved Performance of ALD Coated LiCoO2/Graphite Li-Ion Batteries. *Advanced Energy Materials* **2013**, *3* (2), 213–219. https://doi.org/10.1002/aenm.201200370.
- (18) Jung, Y. S.; Cavanagh, A. S.; Riley, L. a.; Kang, S.-H. H.; Dillon, A. C.; Groner, M. D.; George, S. M.; Lee, S.-H. H. Ultrathin Direct Atomic Layer Deposition on Composite Electrodes for Highly Durable and Safe Li-Ion Batteries. *Advanced Materials* **2010**, *22* (19), 2172–2176. https://doi.org/10.1002/adma.200903951.
- (19) Woo, J. H.; Travis, J. J.; George, S. M.; Lee, S.-H. Utilization of Al₂O₃ Atomic Layer Deposition for Li Ion Pathways in Solid State Li Batteries. *J Electrochem Soc* **2014**, *162* (3), A344–A349. https://doi.org/10.1149/2.0441503jes.
- (20) Jung, S. C.; Han, Y. K. How Do Li Atoms Pass through the Al2O3 Coating Layer during Lithiation in Li-Ion Batteries? *Journal of Physical Chemistry Letters* **2013**, *4* (16), 2681–2685. https://doi.org/10.1021/jz401231e.

- (21) Jung, Y. S.; Cavanagh, A. S.; Dillon, A. C.; Groner, M. D.; George, S. M.; Lee, S.-H. Enhanced Stability of LiCoO[Sub 2] Cathodes in Lithium-Ion Batteries Using Surface Modification by Atomic Layer Deposition. *Journal of The Electrochemical Society* 2010, 157 (1), A75. https://doi.org/10.1149/1.3258274.
- Young, M. J.; Letourneau, S.; Warburton, R. E.; Dose, W. M.; Johnson, C.; Greeley, J.; Elam, J. W. High-Rate Spinel LiMn2O4 (LMO) Following Carbonate Removal and Formation of Li-Rich Interface by ALD Treatment. *The Journal of Physical Chemistry C* **2019**. https://doi.org/10.1021/acs.jpcc.9b04418.
- (23) Darapaneni, P.; Mane, A. U.; Hood, Z. D.; Elam, J. W. Removal of Surface Carbonate from Lithium-Ion Battery Cathode Materials via Vapor-Phase Fluorination. **2022**. https://doi.org/10.1021/acsaem.2c01205.
- (24) Pallister, P. J.; Barry, S. T. Surface Chemistry of Group 11 Atomic Layer Deposition Precursors on Silica Using Solid-State Nuclear Magnetic Resonance Spectroscopy. *Journal of Chemical Physics* **2017**, *146* (052812), 1–10. https://doi.org/10.1063/1.4968021.
- (25) Han, B.; Key, B.; Lipton, A. S.; Vaughey, J. T.; Hughes, B.; Trevey, J.; Dogan, F. Influence of Coating Protocols on Alumina-Coated Cathode Material: Atomic Layer Deposition versus Wet-Chemical Coating. *Journal of The Electrochemical Society* 2019, 166 (15), A3679–A3684. https://doi.org/10.1149/2.0681915jes.
- (26) Lakomaa, E. L.; Root, A.; Suntola, T. Surface Reactions in Al₂O₃ Growth from Trimethylaluminium and Water by Atomic Layer Epitaxy. *Applied Surface Science* **1996**, 107, 107–115. https://doi.org/10.1016/S0169-4332(96)00513-2.
- (27) Kaushik, M.; Leroy, C.; Chen, Z.; Gajan, D.; Willinger, E.; Müller, C. R.; Fayon, F.; Massiot, D.; Fedorov, A.; Copéret, C.; Lesage, A.; Florian, P. Atomic-Scale Structure and Its Impact on Chemical Properties of Aluminum Oxide Layers Prepared by Atomic Layer Deposition on Silica. *Chemistry of Materials* **2021**, *33* (9), 3335–3348. https://doi.org/10.1021/acs.chemmater.1c00516.
- (28) Letourneau, S.; Young, M. J.; Bedford, N. M.; Ren, Y.; Yanguas-Gil, A.; Mane, A. U.; Elam, J. W.; Graugnard, E. Structural Evolution of Molybdenum Disulfide Prepared by Atomic Layer Deposition for Realization of Large Scale Films in Microelectronic Applications. ACS Applied Nano Materials 2018, 1 (8), 4028–4037. https://doi.org/10.1021/acsanm.8b00798.
- (29) He, X.; Waldman, R. Z.; Mandia, D. J.; Jeon, N.; Zaluzec, N. J.; Borkiewicz, O. J.; Ruett, U.; Darling, S. B.; Martinson, A. B. F.; Tiede, D. M. Resolving the Atomic Structure of Sequential Infiltration Synthesis Derived Inorganic Clusters. *ACS Nano* **2020**, *14* (11), 14846–14860. https://doi.org/10.1021/acsnano.0c03848.
- (30) Liu, J.; Li, Z.; Zhang, X.; Otake, K.; Zhang, L.; Peters, A. W.; Young, M. J.; Bedford, N. M.; Letourneau, S. P.; Mandia, D. J.; Elam, J. W.; Farha, O. K.; Hupp, J. T. Introducing

- Nonstructural Ligands to Zirconia-like Metal—Organic Framework Nodes To Tune the Activity of Node-Supported Nickel Catalysts for Ethylene Hydrogenation. *ACS Catalysis* **2019**. https://doi.org/10.1021/acscatal.8b04828.
- (31) Gettler, R. C.; Koenig, H. D.; Young, M. J. Iterative Reverse Monte Carlo and Molecular Statics for Improved Atomic Structure Modeling: A Case Study of Zinc Oxide Grown by Atomic Layer Deposition. *Physical Chemistry Chemical Physics* **2021**, *23* (46), 26417–26427. https://doi.org/10.1039/D1CP03742K.
- (32) Young, M. J.; Bedford, N. M.; Yanguas-Gil, A.; Letourneau, S.; Coile, M.; Mandia, D. J.; Aoun, B.; Cavanagh, A. S.; George, S. M.; Elam, J. W. Probing the Atomic-Scale Structure of Amorphous Aluminum Oxide Grown by Atomic Layer Deposition. *ACS Applied Materials & Interfaces* **2020**, *12* (20), 22804–22814. https://doi.org/10.1021/acsami.0c01905.
- (33) Qu, X.; Yan, D.; Li, R.; Cen, J.; Zhou, C.; Zhang, W.; Lu, D.; Attenkofer, K.; Stacchiola, D. J.; Hybertsen, M. S.; Stavitski, E.; Liu, M. Resolving the Evolution of Atomic Layer-Deposited Thin-Film Growth by Continuous in Situ X-Ray Absorption Spectroscopy. *Chemistry of Materials* **2021**, *33* (5), 1740–1751. https://doi.org/10.1021/acs.chemmater.0c04547.
- (34) Dadlani, A.; Acharya, S.; Trejo, O.; Nordlund, D.; Peron, M.; Razavi, J.; Berto, F.; Prinz, F. B.; Torgersen, J. Revealing the Bonding Environment of Zn in ALD Zn(O,S) Buffer Layers through X-Ray Absorption Spectroscopy. *ACS Applied Materials and Interfaces* **2017**, *9* (45), 39105–39109. https://doi.org/10.1021/acsami.7b06728.
- (35) Kim, Y.; Song, G. Y.; Nandi, R.; Cho, J. Y.; Heo, J.; Cho, D. Y. Phase Identification of Vanadium Oxide Thin Films Prepared by Atomic Layer Deposition Using X-Ray Absorption Spectroscopy. *RSC Advances* **2020**, *10* (44), 26588–26593. https://doi.org/10.1039/d0ra04384b.
- (36) Kokkonen, E.; Kaipio, M.; Nieminen, H. E.; Rehman, F.; Miikkulainen, V.; Putkonen, M.; Ritala, M.; Huotari, S.; Schnadt, J.; Urpelainen, S. Ambient Pressure X-Ray Photoelectron Spectroscopy Setup for Synchrotron-Based in Situ and Operando Atomic Layer Deposition Research. *Review of Scientific Instruments* 2022, 93 (1). https://doi.org/10.1063/5.0076993.
- (37) Kimoto, K.; Matsui, Y.; Nabatame, T.; Yasuda, T.; Mizoguchi, T.; Tanaka, I.; Toriumi, A. Coordination and Interface Analysis of Atomic-Layer-Deposition Al2O3 on Si(001) Using Energy-Loss near-Edge Structures. *Applied Physics Letters* 2003, 83 (21), 4306–4308. https://doi.org/10.1063/1.1629397.
- (38) Jasim, A. M.; He, X.; Xing, Y.; White, T. A.; Young, M. J. Cryo-EPDF: Overcoming Electron Beam Damage to Study the Local Atomic Structure of Amorphous ALD Aluminum Oxide Thin Films within a TEM. *ACS Omega* **2021**, *6* (13), 8986–9000. https://doi.org/10.1021/acsomega.0c06124.

- (39) Hirotsu, Y. Application of Nano-Diffraction to Local Atomic Distribution Function Analysis of Amorphous Materials. *Journal of Electron Microscopy* **2001**, *50* (6), 435–442. https://doi.org/10.1093/jmicro/50.6.435.
- (40) Mu, X.; Mazilkin, A.; Sprau, C.; Colsmann, A.; Kübel, C. Mapping Structure and Morphology of Amorphous Organic Thin Films by 4D-STEM Pair Distribution Function Analysis. *Microscopy* **2019**, *68* (4), 301–309. https://doi.org/10.1093/jmicro/dfz015.
- (41) Jiang, N. Electron Beam Damage in Oxides: A Review. *Reports on Progress in Physics* **2016**, 79 (1), 016501. https://doi.org/10.1088/0034-4885/79/1/016501.
- (42) Baker, L. A.; Rubinstein, J. L. Radiation Damage in Electron Cryomicroscopy. In *Methods in enzymology*; Elsevier Masson SAS, 2010; Vol. 481, pp 371–388. https://doi.org/10.1016/S0076-6879(10)81015-8.
- (43) Spence, J. C. H. Outrunning Damage: Electrons vs X-Rays—Timescales and Mechanisms. *Structural Dynamics* **2017**, *4* (4), 044027. https://doi.org/10.1063/1.4984606.
- (44) Jasim, A.; He, X.; White, T.; Xing, Y. Crystallization of Amorphous Alumina Whiskers on Carbon Nanotubes Under Electron Beam Irradiation. *Microscopy and Microanalysis* **2019**, *25* (S2), 1988–1989. https://doi.org/10.1017/s1431927619010675.
- (45) Groner, M. D.; Fabreguette, F. H.; Elam, J. W.; George, S. M. Low-Temperature Al 2 O 3 Atomic Layer Deposition. *Chemistry of Materials* **2004**, *16* (4), 639–645. https://doi.org/10.1021/cm0304546.
- (46) Young, M. J.; Musgrave, C. B.; George, S. M. Growth and Characterization of Al2O3 Atomic Layer Deposition Films on Sp2-Graphitic Carbon Substrates Using NO2/Trimethylaluminum Pretreatment. *ACS Applied Materials & Interfaces* **2015**, *7* (22), 12030–12037. https://doi.org/10.1021/acsami.5b02167.
- (47) Biskupek, J.; Leschner, J.; Walther, P.; Kaiser, U. Optimization of STEM Tomography Acquisition A Comparison of Convergent Beam and Parallel Beam STEM Tomography. *Ultramicroscopy* **2010**, *110* (9), 1231–1237. https://doi.org/10.1016/j.ultramic.2010.05.008.
- (48) Terban, M. W.; Billinge, S. J. L. Structural Analysis of Molecular Materials Using the Pair Distribution Function. *Chemical Reviews* **2022**, *122* (1), 1208–1272. https://doi.org/10.1021/acs.chemrev.1c00237.
- (49) Elam, J. W.; Groner, M. D.; George, S. M. Viscous Flow Reactor with Quartz Crystal Microbalance for Thin Film Growth by Atomic Layer Deposition. *Review of Scientific Instruments* **2002**, *73* (8), 2981–2987. https://doi.org/10.1063/1.1490410.
- (50) Knözinger, H.; Ratnasamy, P. Catalysis Reviews: Science and Engineering Catalytic Aluminas: Surface Models and Characterization Of. *Catalysis Reviews* **1978**, No. June 2013, 31–70. https://doi.org/10.1080/03602457808080878.

- (51) Zamora, M.; Córdoba, A. A Study of Surface Hydroxyl Groups on γ-Alumina. *Journal of Physical Chemistry* **1978**, 82 (5), 584–588. https://doi.org/10.1021/j100494a017.
- (52) Ott, A. W.; Klaus, J. W.; Johnson, J. M.; George, S. M. Al₂O₃ Thin Film Growth on Si(100) Using Binary Reaction Sequence Chemistry. *Thin Solid Films* **1997**, *292* (1–2), 135–144. https://doi.org/10.1016/S0040-6090(96)08934-1.
- (53) Wertheimer, M. R.; Martinu, L.; Liston, E. M. Handbook of Thin Film Process Technology, Edited by DA Glocker and SI Shah. Institute of Physics, Bristol 1998.
- (54) Dillon, A. C.; Ott, A. W.; Way, J. D.; George, S. M. Surface Chemistry of Al2O3 Deposition Using Al(CH3)3 and H2O in a Binary Reaction Sequence. *Surface Science* **1995**, *322* (1–3), 230–242. https://doi.org/10.1016/0039-6028(95)90033-0.
- (55) Jensen, J. M.; Oelkers, A. B.; Toivola, R.; Johnson, D. C.; Elam, J. W.; George, S. M. X-Ray Reflectivity Characterization of ZnO/Al2O3 Multilayers Prepared by Atomic Layer Deposition. *Chemistry of Materials* **2002**, *14* (5), 2276–2282.
- (56) Jakschik, S.; Schroeder, U.; Hecht, T.; Krueger, D.; Dollinger, G.; Bergmaier, A.; Luhmann, C.; Bartha, J. W. Physical Characterization of Thin ALD-Al2O3 Films. *Applied Surface Science* **2003**, *211* (1–4), 352–359. https://doi.org/10.1016/S0169-4332(03)00264-2.
- (57) Szczygielska, A.; Jabłońska, A.; Burian, A.; Dore, J. C.; Honkimaki, V.; Nagy, J. B. Radial Distribution Function Analysis of Carbon Nanotubes. *Acta Physica Polonica A* **2000**, *98* (5), 611–617. https://doi.org/10.12693/APhysPolA.98.611.
- (58) Hong, S.; van Duin, A. C. T. Molecular Dynamics Simulations of the Oxidation of Aluminum Nanoparticles Using the ReaxFF Reactive Force Field. *The Journal of Physical Chemistry C* **2015**, *119* (31), 17876–17886. https://doi.org/10.1021/acs.jpcc.5b04650.
- (59) Yamaguchi, G.; Yasui, I.; Chiu, W. C. A New Method of Preparing θ-Alumina and the Interpretation of Its X-Ray-Powder Diffraction Pattern and Electron Diffraction Pattern. Bulletin of the Chemical Society of Japan. 1970, pp 2487–2491. https://doi.org/10.1246/bcsj.43.2487.
- (60) Dabaghmanesh, S.; Neyts, E. C.; Partoens, B. Van Der Waals Density Functionals Applied to Corundum-Type Sesquioxides: Bulk Properties and Adsorption of CH 3 and C 6 H 6 on (0001) Surfaces. *Physical Chemistry Chemical Physics* **2016**, *18* (33), 23139–23146. https://doi.org/10.1039/C6CP00346J.
- (61) Song, T. T.; Yang, M.; Chai, J. W.; Callsen, M.; Zhou, J.; Yang, T.; Zhang, Z.; Pan, J. S.; Chi, D. Z.; Feng, Y. P.; Wang, S. J. The Stability of Aluminium Oxide Monolayer and Its Interface with Two-Dimensional Materials. *Scientific Reports* **2016**, *6* (1), 29221. https://doi.org/10.1038/srep29221.

- (62) Wang, X.; Tabakman, S. M.; Dai, H. Atomic Layer Deposition of Metal Oxides on Pristine and Functionalized Graphene. *J Am Chem Soc* **2008**, *130* (26), 8152–8153. https://doi.org/10.1021/ja8023059.
- (63) Brieland-Shoultz, A.; Tawfick, S.; Park, S. J.; Bedewy, M.; Maschmann, M. R.; Baur, J. W.; Hart, A. J. Scaling the Stiffness, Strength, and Toughness of Ceramic-Coated Nanotube Foams into the Structural Regime. *Advanced Functional Materials* **2014**, *24* (36), 5728–5735. https://doi.org/10.1002/adfm.201400851.
- (64) Carter, R.; Davis, B.; Oakes, L.; Maschmann, M. R.; Pint, C. L. A High Areal Capacity Lithium-Sulfur Battery Cathode Prepared by Site-Selective Vapor Infiltration of Hierarchical Carbon Nanotube Arrays. *Nanoscale* **2017**, *9* (39), 15018–15026. https://doi.org/10.1039/c7nr02368e.
- (65) Vervuurt, R. H. J.; Karasulu, B.; Verheijen, M. A.; Kessels, W. M. M.; Bol, A. A. Uniform Atomic Layer Deposition of Al2O3 on Graphene by Reversible Hydrogen Plasma Functionalization. *Chemistry of Materials* **2017**, *29* (5), 2090–2100. https://doi.org/10.1021/acs.chemmater.6b04368.
- (66) Xuan, Y.; Wu, Y. Q.; Shen, T.; Qi, M.; Capano, M. A.; Cooper, J. A.; Ye, P. D. Atomic-Layer-Deposited Nanostructures for Graphene-Based Nanoelectronics. *Applied Physics Letters* 2008, 92 (1), 1–4. https://doi.org/10.1063/1.2828338.
- (67) He, G.; Gao, J.; Chen, H.; Cui, J.; Sun, Z.; Chen, X. Modulating the Interface Quality and Electrical Properties of HfTiO/InGaAs Gate Stack by Atomic-Layer-Deposition-Derived Al2O3 Passivation Layer. *ACS Applied Materials and Interfaces* **2014**, *6* (24), 22013–22025. https://doi.org/10.1021/am506351u.
- (68) Gao, J.; He, G.; Xiao, D.; Jin, P.; Jiang, S.; Li, W.; Liang, S.; Zhu, L. Passivation of Ge Surface Treated with Trimethylaluminum and Investigation of Electrical Properties of HfTiO/Ge Gate Stacks. *Journal of Materials Science and Technology* **2017**, *33* (8), 901–906. https://doi.org/10.1016/j.jmst.2017.04.021.
- (69) He, G.; Chen, X.; Sun, Z. Interface Engineering and Chemistry of Hf-Based High-k Dielectrics on III-V Substrates. *Surface Science Reports* **2013**, *68* (1), 68–107. https://doi.org/10.1016/j.surfrep.2013.01.002.
- (70) Nilsen, O.; Foss, S.; Fjellvåg, H.; Kjekshus, A. Effect of Substrate on the Characteristics of Manganese(IV) Oxide Thin Films Prepared by Atomic Layer Deposition. *Thin Solid Films* **2004**, *468* (1–2), 65–74. https://doi.org/10.1016/j.tsf.2004.04.055.
- (71) Tallarida, M.; Kukli, K.; Michling, M.; Ritala, M.; Leskela, M.; Schmeisser, D. Substrate Reactivity Effects in the Atomic Layer Deposition of Aluminum Oxide from Trimethylaluminum on Ruthenium. *Chemistry of Materials* **2011**, *23* (13), 3159–3168. https://doi.org/10.1021/cm200276z.
- (72) Chen, L.; Connell, J. G.; Nie, A.; Huang, Z.; Zavadil, K. R.; Klavetter, K. C.; Yuan, Y.; Sharifi-Asl, S.; Shahbazian-Yassar, R.; Libera, J. A.; Mane, A. U.; Elam, J. W. Lithium

- Metal Protected by Atomic Layer Deposition Metal Oxide for High Performance Anodes. *J. Mater. Chem. A* **2017**, *5* (24), 12297–12309. https://doi.org/10.1039/C7TA03116E.
- (73) Kozen, A. C.; Lin, C. F.; Pearse, A. J.; Schroeder, M. A.; Han, X.; Hu, L.; Lee, S. B.; Rubloff, G. W.; Noked, M. Next-Generation Lithium Metal Anode Engineering via Atomic Layer Deposition. *ACS Nano* **2015**, *9* (6), 5884–5892. https://doi.org/10.1021/acsnano.5b02166.
- (74) Wilding, M. C.; Benmore, C. J. Structure of Glasses and Melts. *Reviews in Mineralogy and Geochemistry* **2006**, *63* (1), 275–311. https://doi.org/10.2138/rmg.2006.63.12.
- (75) Benmore, C. J. A Review of High-Energy X-Ray Diffraction from Glasses and Liquids. *ISRN Materials Science* **2012**, *2012*, 1–19. https://doi.org/10.5402/2012/852905.
- (76) Petkov, V.; Ren, Y.; Kabekkodu, S.; Murphy, D. Atomic Pair Distribution Functions Analysis of Disordered Low-Z Materials. *Physical Chemistry Chemical Physics* **2013**, *15* (22), 8544–8554.
- (77) Proffen, T.; Billinge, S. J. L.; Egami, T.; Louca, D. Structural Analysis of Complex Materials Using the Atomic Pair Distribution Function a Practical Guide. *Zeitschrift für Kristallographie Crystalline Materials* **2003**, *218* (2), 132–143. https://doi.org/10.1524/zkri.218.2.132.20664.
- (78) Gorelik, T. E.; Neder, R.; Terban, M. W.; Lee, Z.; Mu, X.; Jung, C.; Jacob, T.; Kaiser, U. Towards Quantitative Treatment of Electron Pair Distribution Function. *Acta Crystallographica Section B: Structural Science, Crystal Engineering and Materials* **2019**, 75, 532–549. https://doi.org/10.1107/S205252061900670X.
- (79) McMullan, G.; Faruqi, A. R.; Clare, D.; Henderson, R. Comparison of Optimal Performance at 300 KeV of Three Direct Electron Detectors for Use in Low Dose Electron Microscopy. *Ultramicroscopy* **2014**, *147*, 156–163. https://doi.org/10.1016/J.ULTRAMIC.2014.08.002.
- (80) Clough, R. N.; Moldovan, G.; Kirkland, A. I. Direct Detectors for Electron Microscopy. *Journal of Physics: Conference Series* **2014**, *522* (1), 012046. https://doi.org/10.1088/1742-6596/522/1/012046.
- (81) Bammes, B. E.; Rochat, R. H.; Jakana, J.; Chen, D. H.; Chiu, W. Direct Electron Detection Yields Cryo-EM Reconstructions at Resolutions beyond 3/4 Nyquist Frequency. *Journal of Structural Biology* **2012**, *177* (3), 589–601. https://doi.org/10.1016/J.JSB.2012.01.008.
- (82) Toby, B. H.; von Dreele, R. B. GSAS-II: The Genesis of a Modern Open-Source All Purpose Crystallography Software Package. *Journal of Applied Crystallography* **2013**, *46* (2), 544–549. https://doi.org/10.1107/S0021889813003531.
- (83) Juhás, P.; Davis, T.; Farrow, C. L.; Billinge, S. J. L. PDFgetX3: A Rapid and Highly Automatable Program for Processing Powder Diffraction Data into Total Scattering Pair

- Distribution Functions. *Journal of Applied Crystallography* **2013**, *46* (2), 560–566. https://doi.org/10.1107/S0021889813005190.
- (84) Aoun, B. Fullrmc, a Rigid Body Reverse Monte Carlo Modeling Package Enabled with Machine Learning and Artificial Intelligence. *Journal of Computational Chemistry* **2016**, 37 (12), 1102–1111. https://doi.org/10.1002/jcc.24304.
- (85) Plimpton, S. Fast Parallel Algorithms for Short-Range Molecular Dynamics. *Journal of Computational Physics* **1995**, *117* (1), 1–19. https://doi.org/10.1006/jcph.1995.1039.
- (86) le Roux, S.; Petkov, V. ISAACS-Interactive Structure Analysis of Amorphous and Crystalline Systems. *Journal of Applied Crystallography* **2010**, *43* (1), 181–185. https://doi.org/10.1107/S0021889809051929.

For Table of Contents Only

